1   **Spatial relationships of intra-lesion heterogeneity in *Mycobacterium tuberculosis***

2   **microenvironment, replication status, and drug efficacy**

3

4   Richard C. Lavin[1,2] and Shumin Tan[1,2*]

5

6   [1]Department of Molecular Biology and Microbiology, Tufts University School of Medicine,

7   Boston, Massachusetts, USA.

8   [2]Graduate Program in Molecular Microbiology, Graduate School of Biomedical Sciences, Tufts

9   University, Boston, Massachusetts, USA.

10

11   * Corresponding author

12   E-mail: shumin.tan@tufts.edu

ABSTRACT

A hallmark of *Mycobacterium tuberculosis* (Mtb) infection with critical impact on disease development and outcome is the marked heterogeneity that exists, spanning differences in lesion types to changes in microenvironment as the infection progresses[1-7]. A mechanistic understanding of how this heterogeneity affects Mtb growth and treatment efficacy necessitates single bacterium-level studies in the context of intact host tissue architecture; however, such an evaluation has been technically challenging. Here, we exploit fluorescent reporter Mtb strains and the C3HeB/FeJ murine model in an integrated imaging approach to study microenvironment heterogeneity within a single lesion *in situ*, and analyze how these differences relate to non-uniformity in Mtb replication state, activity, and drug efficacy. We show that the pH and chloride environments differ spatially in a caseous necrotic lesion, with increased acidity and chloride levels in the lesion cuff versus the necrotic core. Conversely, a higher percentage of Mtb in the necrotic core versus the lesion cuff were in an actively replicating state, and correspondingly active in transcription and translation. Finally, examination of three first-line anti-tubercular drugs showed that efficacy of isoniazid was strikingly poor against bacteria in the lesion cuff. Our study reveals spatial relationships of intra-lesion heterogeneity, sheds light on important considerations in the development of anti-tubercular treatment strategies, and establishes a foundational framework for Mtb infection heterogeneity analysis at the single cell level *in situ*.

MAIN TEXT

The ability to effectively treat *Mycobacterium tuberculosis* (Mtb) is significantly impeded by the marked heterogeneity of the infection across multiple levels, including non-uniformity in local microenvironments[1-6]. This heterogeneity extends not just between lesions but within a single

2

36 lesion; for example, matrix-assisted laser desorption/ionization mass spectrometry studies have

37 demonstrated variation in drug penetration into caseous necrotic lesions[8]. Further, pH

38 measurements of liquefying caseum obtained from caseous necrotic lesions in both C3HeB/FeJ

39 mice and guinea pigs have indicated the neutral pH of this material[8,9], which has been contrasted

40 with the slightly acidic pH of the macrophage intraphagosomal environment that is a major niche

41 of the bacterium[10-12]. Of note, the first-line anti-tubercular drug pyrazinamide (PZA) shows

42 increased efficacy in acidic conditions[13-15]. The neutral pH of the caseous material has thus been

43 implicated as a contributing reason for the lack of PZA efficacy sometimes observed in C3HeB/FeJ

44 mice where caseous necrotic lesion types are formed, versus the uniform efficacy observed in

45 BALB/c mice, which do not form caseous necrotic lesions[8,9].

46 The critical impact of within-host heterogeneity on infection and treatment outcome

47 dictates the need to functionally characterize Mtb infection *in vivo* at the single bacterium level,

48 within spatial tissue context. However, the technical hurdles associated with accomplishing such

49 studies has meant a continued dearth in our knowledge of what Mtb actually "sees" during

50 infection at the single bacterium level, and how this may be non-uniform within a host or lesion.

51 In addition, we lack vital information regarding how bacterial growth status may vary in different

52 sublocations within a host. To overcome these challenges and address these key questions, we

53 sought to develop an integrated imaging approach that enables analysis of single bacteria in

54 individual lesions within an infected lung. To establish this approach, we infected C3HeB/FeJ

55 mice with Mtb constitutively expressing mCherry and harvested the lungs 6 weeks post-infection.

56 The utility of C3HeB/FeJ mice as a Mtb infection model has been increasingly appreciated due to

57 its formation of a range of lesion types including caseous necrotic lesions, and it is now frequently

58 used in anti-tubercular drug studies[8,9,16-21]. By employing a broad xy-plane tiled imaging approach

59   coupled with antibody staining against host markers, we were able to distinguish the three lesion

60   types previously described via histological studies in the C3HeB/FeJ murine Mtb infection model

61   (Supplementary Fig. 1)[4,7]. Of particular interest here, highly structured type I caseous necrotic

62   lesions were distinguished by the fibrous collagen I-rich cuff containing CD68-positive

63   macrophages that rings the caseous necrotic core (Supplementary Fig. 1a). Very rare neutrophil-

64   dominant type II lesions were discriminated by Ly6G staining for neutrophils (Supplementary Fig.

65   1b), while macrophage-rich type III lesions were differentiated with CD68 staining of

66   macrophages (Supplementary Fig. 1c). Broad xy-plane tiled imaging provides the breadth required

67   to capture large type I lesions in their entirety (Supplementary Fig. 1a), with subsequent targeted

68   3-dimensional imaging and reconstruction enabling single cell-resolution visualization of the

69   fluorescent bacteria (Supplementary Fig. 1, insets), setting the stage for analysis of intra-lesion

70   sublocation environment and Mtb replication status. We focus here on type I caseous necrotic

71   lesions, due to its association with heterogeneity in drug penetration and Mtb drug response[8,9,16-

72   18,22], and its highly structured nature.

73   We first sought to directly visualize differences in the pH and chloride (Cl$^-$)

74   microenvironment within type I caseous necrotic lesion sublocations, given the reported neutral

75   pH of liquifying caseum[8,9], and our previous work demonstrating the synergistic response of Mtb

76   to pH and Cl$^-$, which are linked cues during macrophage phagosomal maturation[12]. To do so, we

77   infected C3HeB/FeJ mice with our pH/Cl$^-$-responsive fluorescent reporter Mtb strain (Erdman

78   *rv2390c'*::GFP, *smyc'*::mCherry) that fluoresces green upon bacterial exposure to acidic pH and/or

79   high Cl$^-$ levels in the local environment, and expresses mCherry constitutively for visualization of

80   all bacteria irrespective of local environment[12,23]. Comparison of Mtb present in the lesion cuff

81   (predominantly present within macrophages) versus those present in the necrotic lesion core 6-8

82   weeks post-infection showed that the *rv2390c'*::GFP reporter signal was significantly higher in the

83   bacteria present in the lesion cuff (Figs. 1a-1c), even as non-uniformity in reporter signal within

84   each sublocation remained notable (Fig. 1c). Still more strikingly, binning the data for each lesion

85   into different *rv2390c'*::GFP reporter signal ranges demonstrated the opposite distributions in

86   physiological cues experienced by the two bacterial populations (Fig. 1d). Specifically, most Mtb

87   present in the lesion cuff expressed high levels of *rv2390c'*::GFP reporter fluorescence (Figs. 1b-

88   1d), indicative of an environment with more acidic pH and/or higher [Cl⁻], and in accord with the

89   environment that would be expected in macrophage phagosomes[12]. Conversely, a majority of

90   bacteria present in the necrotic core (extracellular Mtb) expressed lower levels of *rv2390c'*::GFP

91   reporter signal (Figs. 1b-1d), indicative of an environment that is at a more neutral pH/has a lower

92   [Cl⁻]. Our findings demonstrate at the single bacterium level within intact tissue that (i) the pH and

93   chloride environment of the caseous necrotic core significantly differs from that experienced by

94   Mtb present within the lesion cuff, and (ii) there remains non-uniformity in the local environment

95   within each sublocation, even in the necrotic core.

96   To understand how this intra-lesion heterogeneity in microenvironment affects Mtb

97   infection and treatment outcome, we next utilized our previously described single-strand DNA-

98   binding protein (SSB)-GFP replication reporter to determine the replication status of Mtb in

99   sublocations within a lesion. In this reporter strain, the Mtb SSB protein is translationally fused to

100 GFP, driven by the native *ssb* promoter, and Mtb undergoing active DNA replication exhibit green

101 foci, providing a proxy for revealing the replication status of a given bacterium[23,24]. Strikingly,

102 analysis of lung tissue from a 6 week C3HeB/FeJ mice infection with the Erdman (SSB-GFP,

103 *smyc'*::mCherry) reporter Mtb strain showed that a significantly greater percentage of Mtb present

104 in the lesion core possessed SSB-GFP foci, indicative of actively replicating bacteria, versus Mtb

5

105   present in the lesion cuff (Fig. 2). This difference in overall replication status between Mtb present

106   in the two lesion sublocations fits with the observed differences in local pH/[Cl⁻] (Fig. 1), with a

107   higher percentage of replicating Mtb in the less harsh environment of the necrotic core. The

108   replication state of Mtb can differentially impact drug efficacy and is implicated as a major

109   contributor to the difficulties of successfully treating Mtb infection, as well as to the necessity for

110   a prolonged treatment time course[25-29]. Yet actual demonstration of how Mtb replication status

111   may differ within a single host during infection has been difficult to establish. Our data presented

112   here provides the first direct evidence, to our knowledge, of how Mtb replication status differs not

113   just within a single host but within a single lesion, and reveals how the non-uniformity in intra-

114   lesion Mtb growth status is spatially related to lesion architecture.

115   The marked difference in bacterial replication state of Mtb residing in the caseous necrotic

116   lesion core versus cuff prompted us to test a second, independent, approach to analyzing Mtb

117   physiological state *in situ*. A dual fluorescent system where one fluorophore is placed under the

118   control of an inducible promoter and a second spectrally distinct fluorophore is expressed

119   constitutively has been successfully utilized to differentiate between transcriptionally active versus

120   non-active Mtb in cultured macrophages[30-32]. We thus applied this strategy here *in vivo*, exploiting

121   a reporter Mtb strain that carries on the chromosome a tetracycline inducible monomeric Kusabira

122   Orange (mKO) construct, along with a constitutively expressed mCherry (P$_{606}$'::mKO-tetON,

123   *smyc'*::mCherry)[30,33]. As an initial test of the system, we infected C3HeB/FeJ mice with the

124   Erdman (P$_{606}$'::mKO-tetONm *smyc'*::mCherry) reporter Mtb strain for one week, before the

125   provision of drinking water containing 5% sucrose $\pm$ 1 mg/ml doxycycline (dox) for one additional

126   week. As shown in Figs. 3a-3c, in this short-term infection, dox treatment resulted in the expected

127   induction of mKO fluorescence in Mtb, with Mtb in the mock-treated mice displaying no mKO

6

128   fluorescence, reinforcing the suitability of dox induction for *in vivo* Mtb studies[34]. To assess spatial

129   intra-lesion differences in Mtb transcriptional/translational activity, we infected C3HeB/FeJ mice

130   with the Erdman (P_{606}'::mKO-tetON, *smyc'*::mCherry) reporter Mtb strain, allowing the infection

131   to establish for 6 weeks prior to a one week exposure of the mice to drinking water containing 5%

132   sucrose + 1 mg/ml dox, and harvesting of lung tissue. A first observation revealed by broad xy-

133   plane imaging was that penetration of dox into the very central core of the caseous necrotic lesion

134   appeared impeded, as no mKO signal could be observed in the bacteria present there

135   (Supplementary Fig. 2). Nonetheless, as mKO signal could be observed within the more peripheral

136   regions of the caseous necrotic core (Supplementary Fig. 2), analysis of the differences in mKO

137   induction in Mtb present in the caseous necrotic core versus cuff was still feasible. Conspicuously,

138   induction of mKO signal was observed in a much greater percentage of Mtb present in the

139   peripheral regions of the caseous necrotic core versus those in the lesion cuff (Figs. 3d and 3e).

140   Additionally, the variation in mKO signal induction within both the cuff and core bacterial

141   populations was significantly greater than that observed in the short-term infection (compare Fig.

142   3b and 3e). These data are consistent with the differences in bacterial replication status between

143   Mtb present in the caseous necrotic core versus cuff, and further supports and highlights the impact

144   of lesion sublocation on Mtb physiological state.

145   The observed differences in pH/Cl⁻ environment and in bacterial replication status and

146   transcriptional/translational activity between Mtb residing in the lesion core versus cuff raised the

147   question of whether anti-tubercular drugs may have differential efficacy even within a single

148   caseous necrotic lesion, separate from lesion penetration issues. To address this question, we

149   infected C3HeB/FeJ mice for 6 weeks with the Erdman (SSB-GFP, *smyc'*::mCherry) reporter Mtb

150   strain, before starting treatment via oral gavage with isoniazid (INH), PZA, or rifampicin (RIF)

151 for two weeks. A control set of infected mice were mock-treated with sterile water. Prominently,

152 consistent with the better efficacy of INH against actively replicating bacteria[35-37], INH treatment

153 was significantly more effective against Mtb present in the caseous necrotic core versus the cuff,

154 with a decrease in the percentage of Mtb with SSB-GFP foci compared to the mock-treated mice

155 in the lesion core (Fig. 4). In contrast, no significant difference in the percentage of Mtb with SSB-

156 GFP foci was observed between the INH and mock-treated groups in the lesion cuff (Fig. 4).

157 In the case of PZA, treatment decreased the percentage of actively replicating Mtb in both

158 lesion sublocations compared to the mock-treated control (Fig. 4b). While PZA has been shown

159 to more efficacious at acidic versus neutral pH[14,15], and the caseous necrotic core has a more neutral

160 pH (Fig. 1)[8,9], it is now also appreciated that PZA can have efficacy in conditions that do not

161 involve non-acidic pH values[38,39]. Our observations here support the concept that PZA has efficacy

162 even within the caseous necrotic core, suggesting that the *in vivo* effect of PZA extends beyond a

163 dependency on local acidic pH conditions. Finally, while RIF treatment showed efficacy against

164 the Mtb population present in both lesion sublocations, it decreased the percentage of Mtb with

165 SSB-GFP foci in the caseous necrotic core to a greater extent (Fig. 4b). RIF acts to inhibit Mtb

166 transcription[40-42], and our findings here are thus in accord with its mode of action.

167 Despite the consensus on the importance of heterogeneity on Mtb infection progression

168 and treatment outcome, population-level readouts such as bacterial load and host cytokine levels

169 continue to be the primary means by which these outcomes are measured. Our establishment here

170 of an integrated imaging approach for *in situ* tissue analysis presents a method to overcome the

171 significant hurdle of the single bacterium resolution required for analysis of Mtb *in vivo* infection

172 heterogeneity. We delineate pH and Cl^- as two facets of the microenvironment that exhibit intra-

173 lesion heterogeneity during Mtb infection, findings that expand on previous studies reporting on

174 the neutral pH of liquefying caseum[8,9], by providing single bacterium resolution analysis in both

175 the lesion cuff and core sublocations, and revealing that heterogeneity in pH and [Cl⁻] is

176 additionally present even within a lesion sublocation. Pimonidazole-based histological labeling

177 has indicated the presence of hypoxia in the cuff of caseous necrotic lesions[22,43], and we anticipate

178 that other vital environmental signals such as nitric oxide are likely to also exhibit intra-lesion

179 heterogeneity. Critically, our data directly demonstrate non-uniformity in bacterial replication

180 status and transcriptional/translational activity within a single lesion, and reveal how these

181 heterogeneous aspects are specifically linked to intra-lesion location. These differences in local

182 environment and Mtb replication and activity further strikingly correlate to spatial differences in

183 drug efficacy that exists even within a single caseous necrotic lesion. This work sets a foundational

184 experimental method and framework for interrogation of (i) the heterogeneity in diverse aspects

185 of Mtb infection biology within and between lesions in a single host, via the use of various reporter

186 Mtb strains[33,44-47], (ii) how drug treatment efficacy may differ in different sublocations within the

187 lung/lesions and/or affect the local environment experienced by the bacterium, and (iii) how

188 targeting of Mtb response to the local environment may change the extent of heterogeneity

189 observed and thereby alter treatment success. We propose that future such single bacterium level

190 studies in the context of intact tissue architecture, perturbing either regulators of bacterial

191 environmental sensing and response or testing the effect of various therapeutic combinations, will

192 build on the groundwork laid here and provide critical mechanistic insight into what drives

193 infection heterogeneity, and how such non-uniformity impacts our ability to successfully treat Mtb

194 infection.

195

196 **METHODS**

Mtb strains and culture

Reporter Mtb strains (*smyc'*::mCherry; *rv2390c'*::GFP, *smyc'*::mCherry; SSB-GFP, *smyc'*::mCherry) used for measuring differences in local microenvironment and replication status were in the Erdman background and have been previously described[12,23]. The P_{606}'::mKO, *smyc'*::mCherry was as previously described[30], except that the construct was placed in the background of the pDE43-MCK backbone, which is an integrating vector[48]. Bacteria were cultured in standing T25 flasks with filter caps, in 7H9 Middlebrook medium supplemented with OADC, 0.05% Tween 80, and 50 μg/ml hygromycin B or 25 μg/ml kanamycin as needed, buffered at pH 7.0 with 100 mM MOPS. Preparation of Mtb stocks for mice infection were as previously described[23].

Ethics statement

All animal procedures followed standards set by the National Institutes of Health "Guide for the Care and Use of Laboratory Animals". Animal protocols were reviewed and approved by the Institutional Animal Care and Use Committee at Tufts University (#B2019-10), in accordance with the Association for Assessment and Accreditation of Laboratory Animal Care, the US Department of Agriculture, and the US Public Health Service guidelines. Light anesthesia during infection and oral gavage administration of drugs was via exposure to 2% isoflurane delivered by a vaporizer system. Euthanasia utilized carbon dioxide gas with regulated flow, consistent with American Veterinary Medical Association guidelines.

Mouse Mtb infections

219   6-8 week old female C3HeB/FeJ wild type mice (Jackson Laboratory, Bar Harbor, ME) were

220   intranasally infected with 10^3 colony forming units of appropriate reporter Mtb strain in 35 µl of

221   phosphate-buffered saline (PBS) containing 0.05% Tween 80, under light anesthesia with 2%

222   isoflurane. Mice were sacrificed at 2, 6, 7, or 8 weeks post-infection, and the lungs fixed overnight

223   in 4% paraformaldehyde (PFA) in PBS, before transfer and storage in PBS prior to analysis. For

224   the P_{606}'::mKO, *smyc'*::mCherry reporter strain infection, infections were allowed to establish for

225   one or six weeks, before provision of the mice with water containing 5% sucrose ± 1 mg/ml

226   doxycycline, with one additional water change during the one week treatment period. For the drug

227   treatment infections, C3HeB/FeJ wild type mice were infected with the SSB-GFP, *smyc'*::mCherry

228   reporter and infection allowed to establish for six weeks, before commencement of treatment with

229   10 mg/kg isoniazid (INH), 150 mg/kg pyrazinamide (PZA), or 10 mg/kg rifampicin (RIF) via oral

230   gavage five times a week for 2 weeks (in a 200 µl volume). Control infected mice were mock-

231   treated with sterile water. All drugs were prepared weekly, and all oral gavage treatments were

232   carried out under light anesthesia with 2% isoflurane. INH and PZA working solutions were

233   prepared directly in sterile water. RIF working solution was prepared by diluting 50 mg/ml RIF

234   stock in DMSO to 10 mg/kg RIF + 5% DMSO in sterile water.

235

236   **Confocal immunofluorescence microscopy**

237   Fixed lung lobes were embedded in 4% agarose in PBS and 250 µm sections obtained with a Leica

238   VT1000S vibratome[49]. Staining of tissue was essentially as previously described[12,23,49] – lung

239   sections were blocked and permeabilized in PBS + 3% BSA + 0.1% Triton X-100 ("blocking

240   buffer") for 1 hour at room temperature, before incubation with primary antibodies overnight at

241   room temperature (all steps on a nutator). The next morning, samples were washed 3 x 5 minutes

242 with blocking buffer, then incubated with secondary antibodies at room temperature for 2 hours

243 (all steps on a nutator). Samples were washed 3 x 5 minutes with blocking buffer again, and

244 mounted with Vectashield mounting medium (Vector labs, Burlingame, CA). Rabbit anti-collagen

245 I (Novus Biologicals, Centennial, CO, catalog #NB600-408) was used at 1:250, and Alexa Fluor

246 514 goat anti-rabbit (Invitrogen, Carlsbad, CA, catalog #A31558) used at 1:200 for secondary

247 detection. Rat anti-CD68 (Bio-Rad, Hercules, CA, catalog #MCA1957) and rat anti-Ly6G (BD

248 Biosciences, San Jose, CA, catalog #551459) were each used at 1:100, and Alexa Fluor 647 goat

249 anti-rat (Invitrogen, catalog #A21247) used at 1:100 for secondary detection. Nuclei were

250 visualized with DAPI (1:500; Invitrogen, catalog #D3571). Samples were imaged on a Leica SP8

251 spectral confocal microscope.

252 For broad xy-plane imaging, the Leica LAS X Navigator module was used to obtain

253 multiple overlapping images that were then automatically merged together. High resolution images

254 for reporter quantification were 10 μm in depth, reconstructed into 3D using Volocity software

255 (Quorum Technologies, Ontario, Canada) from images taken at 0.5 μm z-steps. Quantification of

256 reporter signal was carried out essentially as previously described using Volocity software[12,23,49].

257 In brief, for the *rv2390c'*::GFP reporter, the volume of each bacterium was measured via the

258 mCherry channel, and the corresponding total GFP signal for that given object (bacterium)

259 simultaneously measured. The settings for the GFP channel were maintained across samples to

260 allow for comparison of values. Statistical analysis was performed using a Mann-Whitney test for

261 comparison of reporter signal in bacteria present in the cuff versus core region in each lesion. A

262 multiple t-test with a Holm-Sidak correction was used for statistical analysis of the binned data of

263 reporter signal in the cuff versus core across all lesions. The P_{606}'::mKO, *smyc'*::mCherry reporter

264 strain was quantified in the same manner as for the *rv2390c'*::GFP reporter. For the SSB-GFP

265   reporter, individual bacteria were identified via the mCherry channel and the number of bacteria

266   with SSB-GFP puncta determined. Numbers of bacteria quantified in each case are indicated in

267   the figure legends. Statistical analysis was performed using a Wilcoxon matched-pairs signed rank

268   test for comparison of lesion cuff versus core values, and with a Mann-Whitney statistical test for

269   comparing drug to mock treatment in a lesion sublocation.

270

271   **DATA AVAILABILITY**

272   All relevant data are within the paper and its supplementary files.

273

274   **ACKNOWLEDGEMENTS**

283

284   **REFERENCES**

285   1   Aldridge, B. B. *et al.* Asymmetry and aging of mycobacterial cells lead to variable growth and

286   antibiotic susceptibility. *Science* **335**, 100-104 (2012).

287   2   Cadena, A. M., Fortune, S. M. & Flynn, J. L. Heterogeneity in tuberculosis. *Nat Rev Immunol*

288   **17**, 691-702 (2017).

289   3   Lanoix, J. P., Lenaerts, A. J. & Nuermberger, E. L. Heterogeneous disease progression and

290   treatment response in a C3HeB/FeJ mouse model of tuberculosis. *Dis Model Mech* **8**, 603-610

291   (2015).

292   4   Lenaerts, A., Barry, C. E., 3rd & Dartois, V. Heterogeneity in tuberculosis pathology,

293   microenvironments and therapeutic responses. *Immunol Rev* **264**, 288-307 (2015).

294   5   Manina, G., Dhar, N. & McKinney, J. D. Stress and host immunity amplify *Mycobacterium*

295   *tuberculosis* phenotypic heterogeneity and induce nongrowing metabolically active forms. *Cell*

296   *Host Microbe* **17**, 32-46 (2015).

297   6   Mattila, J. T. *et al.* Microenvironments in tuberculous granulomas are delineated by distinct

298   populations of macrophage subsets and expression of nitric oxide synthase and arginase

299   isoforms. *J Immunol* **191**, 773-784 (2013).

300   7   Irwin, S. M. *et al.* Presence of multiple lesion types with vastly different microenvironments

301   in C3HeB/FeJ mice following aerosol infection with *Mycobacterium tuberculosis*. *Dis Model*

302   *Mech* **8**, 591-602 (2015).

303   8   Irwin, S. M. *et al.* Bedaquiline and pyrazinamide treatment responses are affected by

304   pulmonary lesion heterogeneity in *Mycobacterium tuberculosis*i infected C3HeB/FeJ mice.

305   *ACS Infect Dis* **2**, 251-267 (2016).

306   9   Lanoix, J. P. *et al.* Selective inactivity of pyrazinamide against tuberculosis in C3HeB/FeJ

307   mice is best explained by neutral pH of caseum. *Antimicrob Agents Chemother* **60**, 735-743

308   (2016).

14

309   10 Pethe, K. *et al.* Isolation of *Mycobacterium tuberculosis* mutants defective in the arrest of

310   phagosome maturation. *Proc Natl Acad Sci USA* **101**, 13642-13647 (2004).

311   11 Rohde, K. H., Abramovitch, R. B. & Russell, D. G. *Mycobacterium tuberculosis* invasion of

312   macrophages: linking bacterial gene expression to environmental cues. *Cell Host Microbe* **2**,

313   352-364 (2007).

314   12 Tan, S., Sukumar, N., Abramovitch, R. B., Parish, T. & Russell, D. G. *Mycobacterium*

315   *tuberculosis* responds to chloride and pH as synergistic cues to the immune status of its host

316   cell. *PLoS Pathog* **9**, e1003282 (2013).

317   13 Salfinger, M. & Heifets, L. B. Determination of pyrazinamide MICs for *Mycobacterium*

318   *tuberculosis* at different pHs by the radiometric method. *Antimicrob Agents Chemother* **32**,

319   1002-1004 (1988).

320   14 Zhang, Y., Scorpio, A., Nikaido, H. & Sun, Z. Role of acid pH and deficient efflux of

321   pyrazinoic acid in unique susceptibility of *Mycobacterium tuberculosis* to pyrazinamide. *J*

322   *Bacteriol* **181**, 2044-2049 (1999).

323   15 Zhang, Y., Shi, W., Zhang, W. & Mitchison, D. Mechanisms of pyrazinamide action and

324   resistance. *Microbiol Spectr* **2**, Mgm2-0023-2013 (2014).

325   16 Driver, E. R. *et al.* Evaluation of a mouse model of necrotic granuloma formation using

326   C3HeB/FeJ mice for testing of drugs against *Mycobacterium tuberculosis*. *Antimicrob Agents*

327   *Chemother* **56**, 3181-3195 (2012).

328   17 Irwin, S. M. *et al.* Limited activity of clofazimine as a single drug in a mouse model of

329   tuberculosis exhibiting caseous necrotic granulomas. *Antimicrob Agents Chemother* **58**, 4026-

330   4034 (2014).

331   18 Lanoix, J. P., Betoudji, F. & Nuermberger, E. Sterilizing activity of pyrazinamide in

332   combination with first-line drugs in a C3HeB/FeJ mouse model of tuberculosis. *Antimicrob*

333   *Agents Chemother* **60**, 1091-1096 (2016).

334   19 Lavin, R. C. *et al.* Targeting *Mycobacterium tuberculosis* response to environmental cues for

335   the development of effective antitubercular drugs. *PLoS Biol* **19**, e3001355 (2021).

336   20 Ordonez, A. A. *et al.* Matrix metalloproteinase inhibition in a murine model of cavitary

337   tuberculosis paradoxically worsens pathology. *J Infect Dis* **219**, 633-636 (2019).

338   21 Robertson, G. T. *et al.* Spectinamides are effective partner agents for the treatment of

339   tuberculosis in multiple mouse infection models. *J Antimicrob Chemother* **72**, 770-777 (2017).

340   22 Harper, J. *et al.* Mouse model of necrotic tuberculosis granulomas develops hypoxic lesions. *J*

341   *Infect Dis* **205**, 595-602 (2012).

342   23 Sukumar, N., Tan, S., Aldridge, B. B. & Russell, D. G. Exploitation of *Mycobacterium*

343   *tuberculosis* reporter strains to probe the impact of vaccination at sites of infection. *PLoS*

344   *Pathog* **10**, e1004394 (2014).

345   24 Huang, L., Nazarova, E. V., Tan, S., Liu, Y. & Russell, D. G. Growth of *Mycobacterium*

346   *tuberculosis in vivo* segregates with host macrophage metabolism and ontogeny. *J Exp Med*

347   **215**, 1135-1152 (2018).

348   25 Caño-Muñiz, S., Anthony, R., Niemann, S. & Alffenaar, J. C. New approaches and therapeutic

349   options for *Mycobacterium tuberculosis* in a dormant state. *Clin Microbiol Rev* **31**, e00060-17

350   (2018).

351   26 Gomez, J. E. & McKinney, J. D. M. tuberculosis persistence, latency, and drug tolerance.

352   *Tuberculosis (Edinb)* **84**, 29-44 (2004).

16

353   27 Horsburgh, C. R., Jr., Barry, C. E., 3rd & Lange, C. Treatment of tuberculosis. *N Engl J Med*

354   **373**, 2149-2160 (2015).

355   28 Karakousis, P. C. *et al.* Dormancy phenotype displayed by extracellular *Mycobacterium*

356   *tuberculosis* within artificial granulomas in mice. *J Exp Med* **200**, 647-657 (2004).

357   29 Wayne, L. G. & Sohaskey, C. D. Nonreplicating persistence of *Mycobacterium tuberculosis*.

358   *Annu Rev Microbiol* **55**, 139-163 (2001).

359   30 Huang, L. *et al.* The deconstructed granuloma: a complex high-throughput drug screening

360   platform for the discovery of host-directed therapeutics against tuberculosis. *Front Cell Infect*

361   *Microbiol* **8**, 275 (2018).

362   31 Martin, C. J. *et al.* Efferocytosis is an innate antibacterial mechanism. *Cell Host Microbe* **12**,

363   289-300 (2012).

364   32 Mouton, J. M., Helaine, S., Holden, D. W. & Sampson, S. L. Elucidating population-wide

365   mycobacterial replication dynamics at the single-cell level. *Microbiology* **162**, 966-978 (2016).

366   33 MacGilvary, N. J. & Tan, S. Fluorescent *Mycobacterium tuberculosis* reporters: illuminating

367   host-pathogen interactions. *Pathog Dis* **76**, fty017 (2018).

368   34 Gandotra, S., Schnappinger, D., Monteleone, M., Hillen, W. & Ehrt, S. *In vivo* gene silencing

369   identifies the *Mycobacterium tuberculosis* proteasome as essential for the bacteria to persist in

370   mice. *Nat Med* **13**, 1515-1520 (2007).

371   35 Baek, S. H., Li, A. H. & Sassetti, C. M. Metabolic regulation of mycobacterial growth and

372   antibiotic sensitivity. *PLoS Biol* **9**, e1001065 (2011).

373   36 Bellerose, M. M. *et al.* Distinct bacterial pathways influence the efficacy of antibiotics against

374   *Mycobacterium tuberculosis*. *mSystems* **5**, e00396-20 (2020).

375   37 Dhar, N. & McKinney, J. D. *Mycobacterium tuberculosis* persistence mutants identified by

376   screening in isoniazid-treated mice. *Proc Natl Acad Sci USA* **107**, 12275-12280 (2010).

377   38 den Hertog, A. L. *et al.* Pyrazinamide is active against *Mycobacterium tuberculosis* cultures at

378   neutral pH and low Temperature. *Antimicrob Agents Chemother* **60**, 4956-4960 (2016).

379   39 Peterson, N. D., Rosen, B. C., Dillon, N. A. & Baughn, A. D. Uncoupling environmental pH

380   and intrabacterial acidification from pyrazinamide susceptibility in *Mycobacterium*

381   *tuberculosis*. *Antimicrob Agents Chemother* **59**, 7320-7326 (2015).

382   40 Levin, M. E. & Hatfull, G. F. *Mycobacterium smegmatis* RNA polymerase: DNA supercoiling,

383   action of rifampicin and mechanism of rifampicin resistance. *Mol Microbiol* **8**, 277-285 (1993).

384   41 Boyaci, H., Saecker, R. M. & Campbell, E. A. Transcription initiation in mycobacteria: a

385   biophysical perspective. *Transcription* **11**, 53-65 (2020).

386   42 Somoskovi, A., Parsons, L. M. & Salfinger, M. The molecular basis of resistance to isoniazid,

387   rifampin, and pyrazinamide in *Mycobacterium tuberculosis*. *Respir Res* **2**, 164-168 (2001).

388   43 Via, L. E. *et al.* Tuberculous granulomas are hypoxic in guinea pigs, rabbits, and nonhuman

389   primates. *Infect Immun* **76**, 2333-2340 (2008).

390   44 Bhaskar, A. *et al.* Reengineering redox sensitive GFP to measure mycothiol redox potential of

391   *Mycobacterium tuberculosis* during infection. *PLoS Pathog* **10**, e1003902 (2014).

392   45 Jain, P. *et al.* Dual-reporter mycobacteriophages (Φ2DRMs) reveal preexisting *Mycobacterium*

393   *tuberculosis* persistent cells in human sputum. *mBio* **7**, e01023-16 (2016).

394   46 MacGilvary, N. J., Kevorkian, Y. L. & Tan, S. Potassium response and homeostasis in

395   *Mycobacterium tuberculosis* modulates environmental adaptation and is important for host

396   colonization. *PLoS Pathog* **15**, e1007591 (2019).

397   47 Nazarova, E. V. *et al.* Rv3723/LucA coordinates fatty acid and cholesterol uptake in

398   *Mycobacterium tuberculosis*. *Elife* **6**, e26969 (2017).

399   48 Kim, J. H. *et al.* A genetic strategy to identify targets for the development of drugs that prevent

400   bacterial persistence. *Proc Natl Acad Sci USA* **110**, 19095-19100 (2013).

401   49 Giacalone, D., Huang, L. & Tan, S. Exploiting fluorescent proteins to understand

402   *Mycobacterium tuberculosis* biology. *Methods Mol Biol* **2314**, 365-383 (2021).

Figure 1
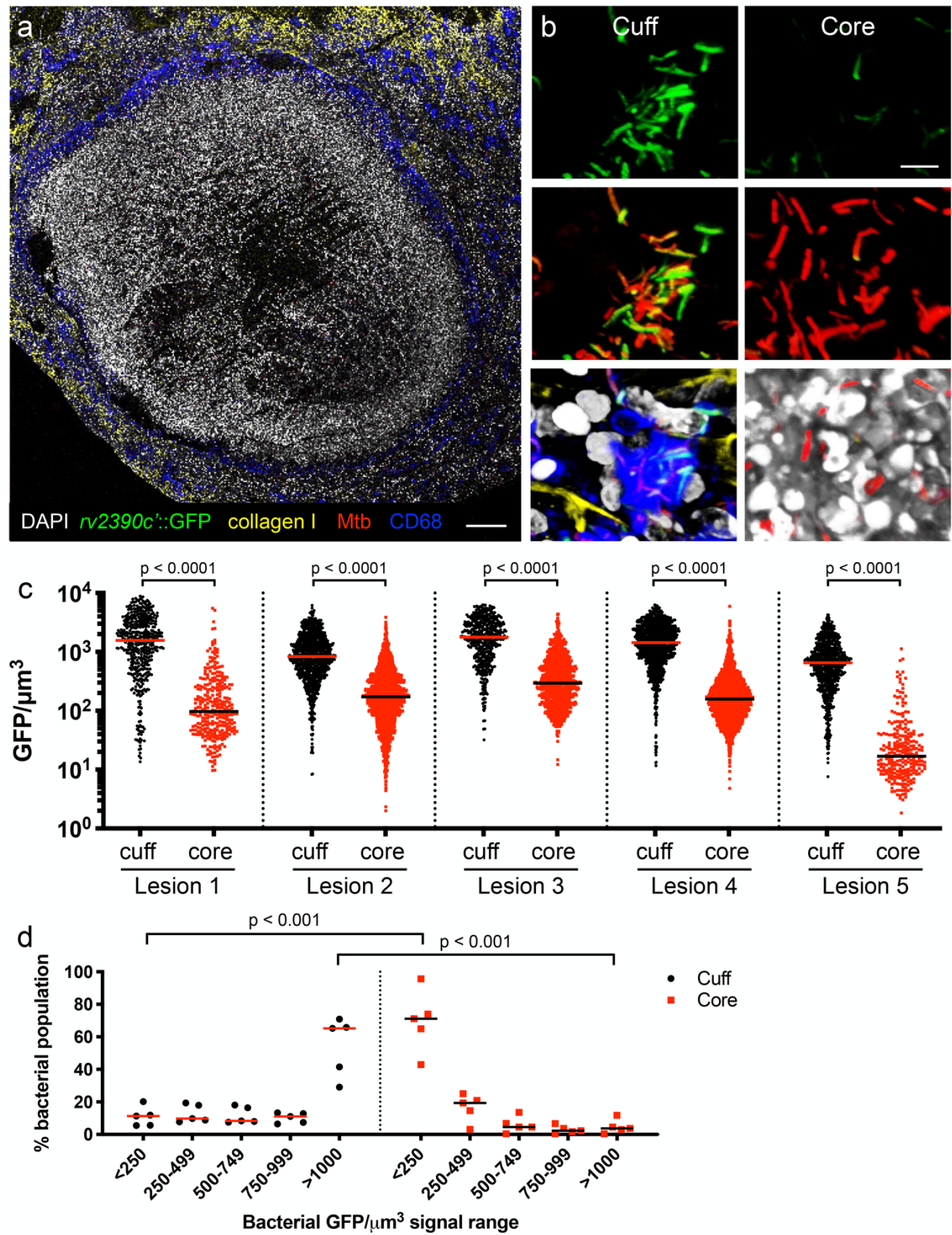
Fig. 1. *rv2390c'*::**GFP reporter reveals heterogeneity in pH/Cl⁻ levels within different sublocations of caseous necrotic lesions.** (a and b) Confocal microscopy images of type I caseous necrotic lesions from 6-8 week infection of C3HeB/FeJ mice with Erdman (*rv2390c'*::GFP, *smyc'*::mCherry). Overview image of a lesion (~10 x 11 tiled image) is shown in (a), and representative 3D confocal images from the lesion cuff and core shown in (b). All bacteria are marked in red (*smyc'*::mCherry), reporter signal is shown in green (*rv2390c'*::GFP), nuclei are shown in grayscale (DAPI), collagen I is shown in yellow, and macrophages are shown in blue (CD68). Scale bar 200 μm in (a) and 5 μm in (b). (c) shows GFP/μm³ signal for individual bacteria or a group of tightly clustered bacteria, quantified from multiple 3D confocal images at each lesion sublocation (5 different lesions from 5 mice; number of bacteria quantified was respectively 478, 307, 937, 1715, 516, 885, 1078, 1755, 749, and 257 for each lesion sublocation as shown from left to right on the graph). Horizontal lines mark the median value for each sample. p-values were obtained with a Mann-Whitney statistical test. (d) shows data from (c) binned into 5 sub-ranges of GFP/μm³ signal. Each point on the graph represents one lesion. Horizontal lines mark the median value for each group. p-values were obtained with a multiple t-test with a Holm-Sidak correction.

Figure 2
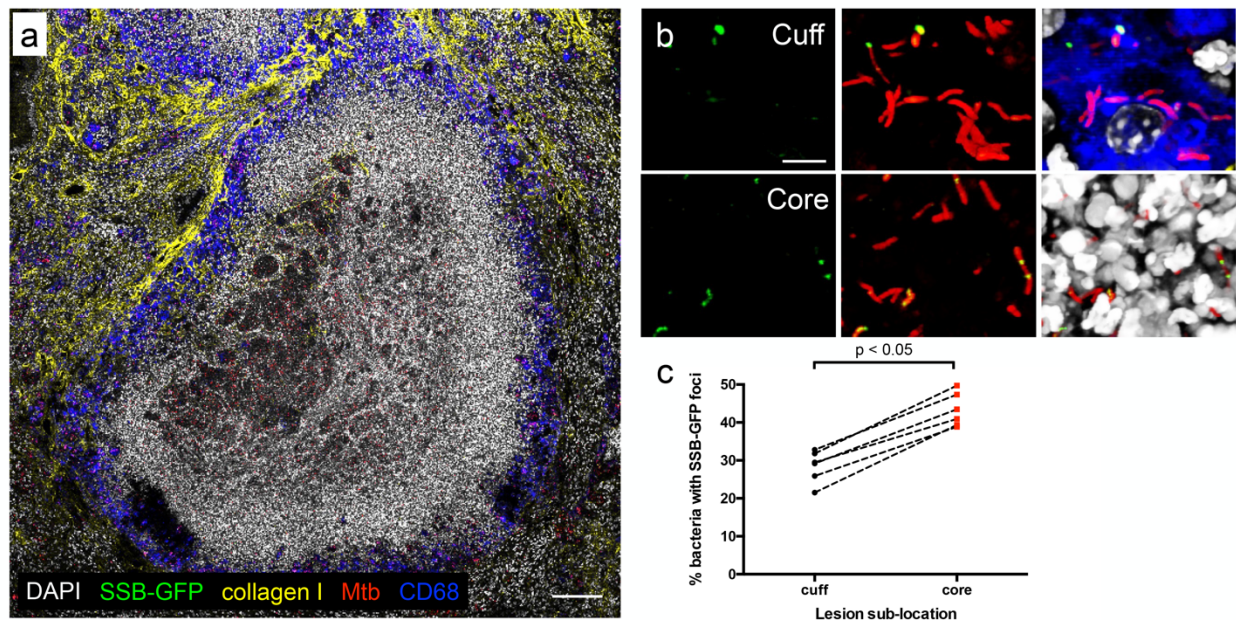
Fig. 2. SSB-GFP reporter reveals heterogeneity in bacterial replication within different sublocations of caseous necrotic lesions. (a and b) Confocal microscopy images of type I caseous necrotic lesions from 6 week infection of C3HeB/FeJ mice with Erdman (SSB-GFP, *smyc'*::mCherry). Overview image of a lesion (~5 x 5 tiled image) is shown in (a), and representative 3D confocal images from the lesion cuff and core are shown in (b). All bacteria are marked in red (*smyc'*::mCherry), reporter signal is shown in green (SSB-GFP), nuclei are shown in grayscale (DAPI), collagen I is shown in yellow, and macrophages are shown in blue (CD68). For clarity of foci visualization, SSB-GFP signal is shown in extended focus, overlaid on the 3D images in (b). Scale bar 100 μm in (a) and 5 μm in (b). (c) shows the percentage of Mtb displaying SSB-GFP foci in each lesion sublocation for each quantified lesion measured from multiple 3D confocal images (6 different lesions from 5 mice; number of bacteria quantified in each lesion sublocation [cuff, core] was [678, 475], [564, 545], [370, 446], [478, 1248], [537, 867], and [393, 360]). p-value was obtained using a Wilcoxon matched-pairs signed rank test.

Figure 3
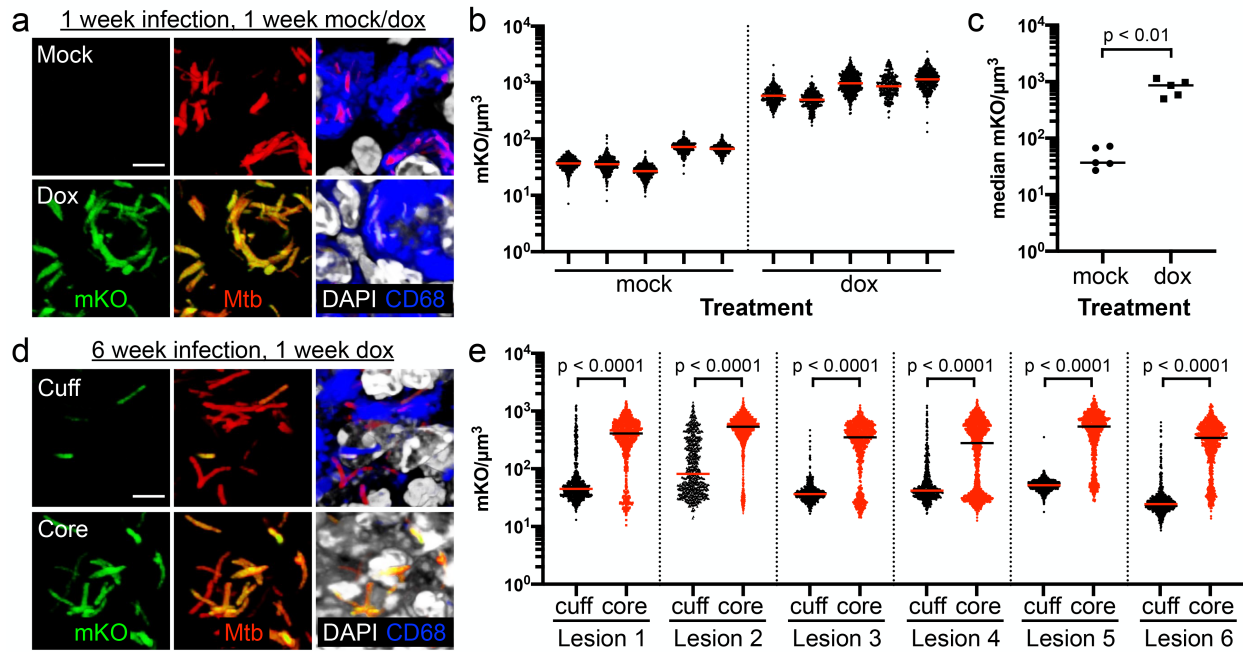
Fig. 3. Heterogeneity in bacterial transcriptional/translational activity within different sublocations of caseous necrotic lesions. (a) Representative 3D confocal images from the lesion cuff and core from a 1 week infection of C3HeB/FeJ mice with Erdman (P$_{606}$'::mKO-tetON, *smyc'*::mCherry), followed by 1 week of exposure to drinking water ± 1 mg/ml doxycycline. All bacteria are marked in red (*smyc'*::mCherry), reporter signal is shown in green (P$_{606}$'::mKO-tetON), nuclei are shown in grayscale (DAPI), and macrophages are shown in blue (CD68). Scale bar 5 μm. (b) mKO/μm^3 signal for individual bacteria or a group of tightly clustered bacteria, quantified from multiple 3D confocal images from infections as performed in (a) (5 different mice/treatment group; number of bacteria quantified from each sample was respectively 440, 424, 604, 379, 436, 355, 330, 545, 257, and 425 as shown from left to right on the graph). Horizontal lines mark the median value for each sample. (c) graphs the medians of each sample shown in (b), with p-value obtained with a Mann-Whitney statistical test. (d) Representative 3D confocal images from the lesion cuff and core from a 6 week infection of C3HeB/FeJ mice with Erdman

(P$_{606}$'::mKO-tetON, *smyc'*::mCherry), followed by 1 week of exposure to drinking water + 1 mg/ml doxycycline. All bacteria are marked in red (*smyc'*::mCherry), reporter signal is shown in green (P$_{606}$'::mKO-tetON), nuclei are shown in grayscale (DAPI), and macrophages are shown in blue (CD68). Scale bar 5 μm. (e) mKO/μm^3 signal for individual bacteria or a group of tightly clustered bacteria, quantified from multiple 3D confocal images at each lesion sublocation (6 different lesions from 5 mice; number of bacteria quantified was respectively 612, 745, 728, 1802, 488, 913, 636, 1615, 1527, 1058, 599, and 921, for each lesion sublocation as shown from left to right on the graph). Horizontal lines mark the median value for each sample. p-values were obtained with a Mann-Whitney statistical test.

Figure 4
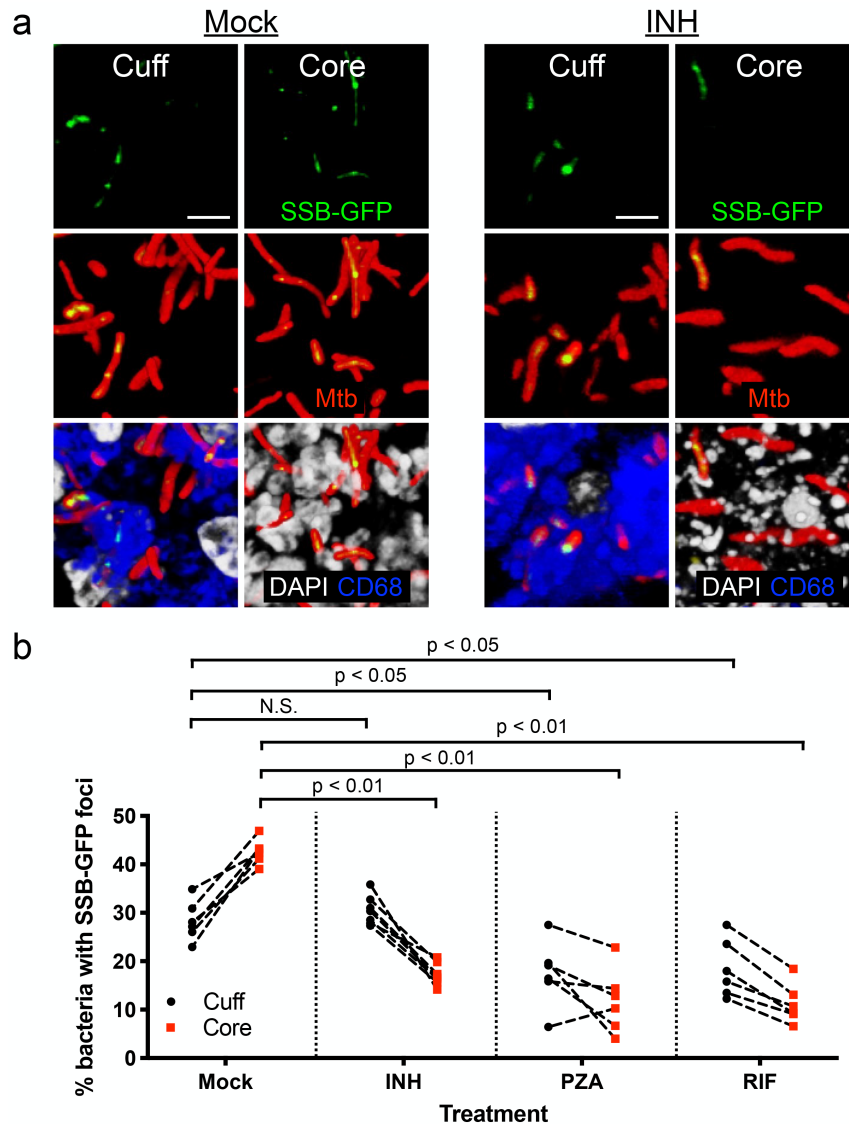
Fig. 4. Impact of bacterial sublocation within caseous necrotic lesions on efficacy of first-line antitubercular drugs. (a) Representative 3D confocal images from the lesion cuff and core from a 6 week infection of C3HeB/FeJ mice with Erdman (SSB-GFP, *smyc'*::mCherry), followed by 2 weeks of mock or 10 mg/kg isoniazid (INH) treatment. All bacteria are marked in red (*smyc'*::mCherry), reporter signal is shown in green (SSB-GFP), nuclei are shown in grayscale (DAPI), and macrophages are shown in blue (CD68). For clarity of foci visualization, SSB-GFP signal is shown in extended focus, overlaid on the 3D images. Scale bar 5 μm. (b) shows the

percentage of Mtb displaying SSB-GFP foci in each lesion sublocation for each quantified lesion, measured from multiple 3D confocal images for each set of 6 week infections followed by 2 weeks of mock, 10 mg/kg INH, 150 mg/kg pyrazinamide (PZA), or 10 mg/kg rifampicin (RIF) treatment. p-values were obtained with a Mann-Whitney statistical test. Sample details are as follows: mock treatment set – 6 different lesions from 5 mice; number of bacteria quantified in each lesion sublocation [cuff, core] was [641, 891], [481, 389], [408, 339], [318, 367], [447, 425], and [541, 453]. INH treatment set – 7 different lesions from 4 mice; number of bacteria quantified in each lesion sublocation [cuff, core] was [319, 371], [371, 467], [417, 385], [450, 403], [412, 419], [339, 311], and [368, 339]. PZA treatment set – 6 different lesions from 5 mice; number of bacteria quantified in each lesion sublocation [cuff, core] was [219, 210], [423, 626], [418, 543], [248, 419], [285, 366], and [341, 375]. RIF treatment set – 6 different lesions from 4 mice; number of bacteria quantified in each lesion sublocation [cuff, core] was [215, 297], [300, 151], [246, 275], [212, 122], [318, 378], and [367, 215].